ChemComm

COMMUNICATION

View Article Online
View Journal | View Issue

Published on 29 January 2020. Downloaded by WUHAN UNIVERSITY OF TECHNOLOGY on 4/7/2020 9:24:58 AM.

Check for updates

Cite this: *Chem. Commun.*, 2020, **56**, 2751

Received 9th December 2019,
Accepted 29th January 2020

DOI: 10.1039/c9cc09558f

rsc.li/chemcomm

Ternary TiO_2/SiO_x@C nanocomposite derived from a novel titanium–silicon MOF for high-capacity and stable lithium storage†

Wenchao Shi, Jiashen Meng, Qi Li,* Zhitong Xiao, Xiaoming Xu, Mingsheng Qin, Xiao Zhang and Liqiang Mai

A novel titanium–silicon MOF precursor was first designed and constructed *via* a facile solvothermal process. After subsequent pyrolysis, the derived ternary TiO_2/SiO_x@C nanocomposite exhibited superior lithium storage performances, which was attributed to their all-in-one architecture of synergistic components, including stable-cycling nanostructured TiO_2, high-capacity SiO_x and high-conductivity carbon matrix.

Titanium dioxide (TiO_2) is an anode material with great promise for lithium-ion batteries (LIBs) on account of its characteristics including abundant resources, high safety and environmental benignity. Besides, TiO_2 as electrode materials exhibit long-cycle stability due to its stable chemical structure and small volume change (<4%) during lithiation/delithiation process.[1] However, the further application of TiO_2 electrodes in LIBs is hampered by two fatal issues: (1) unsatisfactory rate capability arising from low electronic conductivity and ionic diffusivity; (2) low theoretical capacity (335 mA h g^{-1}). To address the poor rate performance of TiO_2 electrodes, one common approach is to design and construct nanostructured TiO_2 to enlarge the electrode/electrolyte interface and shorten lithium ion (Li^+) diffusion pathway.[2] Another efficient strategy is to combine TiO_2 with materials which possesses good electronic conductivity, such as carbon materials.[3] For instance, Zhang *et al.* obtained tiny anatase TiO_2 nanocrystals encapsulated under thin conductive carbon layer, which exhibits high-rate lithium storage with a reversible capacity of 127 mA h g^{-1} at 3.35 A g^{-1}.[4] With respect to the low capacity, combining TiO_2 with high-capacity metal oxide is the most adopted method, such as SnO_2,[5] CoO,[6] Co_3O_4,[7] and MnO_2[8] *etc.* These binary composites deliver significantly increased capacities, while retaining the intrinsic merits of TiO_2. Compared with these metal oxides, silicon suboxide (SiO_x, $0 < x < 2$) has attracted more attention in recent years because of its higher theoretical capacity, lower price and environmental friendliness.[9,10] Therefore, it is expected to be an efficient approach to resolve the above-mentioned problems of TiO_2 electrodes through constructing ternary nanocomposite consisted of stable-cycling nanostructured TiO_2, conductive carbon material and high-capacity SiO_x.

Recently, metal–organic frameworks (MOFs) have been extensively used as precursors to fabricate various multi-component carbon-confined metal–oxide composite materials, which tend to show excellent electrochemical properties owing to their inheriting unique architectures from MOFs precursors.[11,12] In this regard, Yang *et al.* obtained porous carbon-confined ZnO quantum dots with high ionic diffusivity and electronic conductivity through calcinating a MOF precursor, which showed an outstanding lithium storage performance.[13] Moreover, Sun *et al.* developed Fe–Mn–O/C nanocomposite *via* carbonizing the bimetal-organic framework of Fe/Mn-MOF-74, and it exhibited excellent electrochemical performance in lithium storage owing to the synergistic effect of ternary components.[14] Therefore, designing and constructing novel MOFs as the precursors represents an effective and important method to prepare multi-component synergistic nanocomposites with high-efficiency energy storage.

Herein, a novel titanium–silicon MOF (Ti–Si MOF) was first developed through a simple solvothermal process, in which titanium source and silicon source with the similar coordinative state were selected. After subsequent controlled pyrolysis, ternary carbon-confined TiO_2/SiO_x nanocomposite (denoted as TiO_2/SiO_x@C) was obtained. In this ternary architecture, anatase TiO_2 nanocrystallites and amorphous SiO_x are embedded in the carbon matrix to form an inner core, which is entirely encapsulated in an amorphous carbon shell. As the result of this unique MOF-derived architecture, the ternary TiO_2/SiO_x@C nanocomposite showed high electronic conductivity, abundant hierarchical pores, and stable structure. When tested as an anode material for LIBs, the as-synthesized TiO_2/SiO_x@C not only delivered a fairly high capacity (647 mA h g^{-1} at 0.1 A g^{-1}), but also exhibited satisfying long-cycle stability (capacity retention of 78% after 500 cycles) and superior rate capability (401 mA h g^{-1} at 5 A g^{-1}).

State Key Laboratory of Advanced Technology for Materials Synthesis and Processing, Wuhan University of Technology, Wuhan 430070, China.
E-mail: qi.li@whut.edu.cn

† Electronic supplementary information (ESI) available. See DOI: 10.1039/c9cc09558f

Published on 29 January 2020. Downloaded by WUHAN UNIVERSITY OF TECHNOLOGY on 4/7/2020 9:24:58 AM.

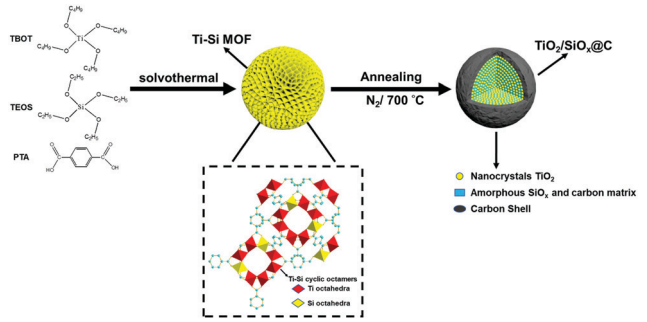

Fig. 1 Schematic illustration of the formation mechanism of TiO_2/SiO_x@C ternary nanocomposite.

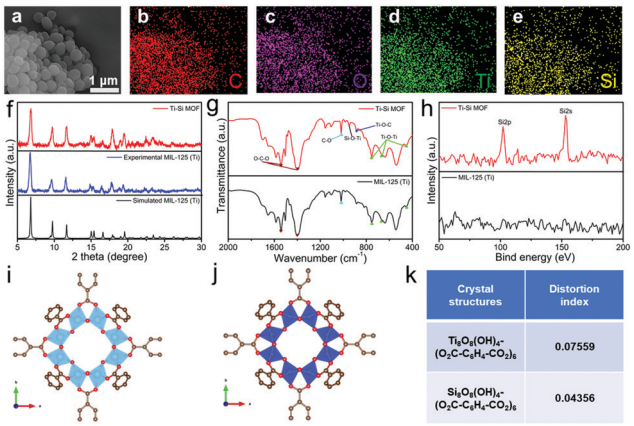

Fig. 2 Characterization of Ti–Si MOF and MIL-125 (Ti). (a) SEM images of Ti–Si MOF, and EDX elemental mappings of C, O, Ti and Si (b–e) of Ti-Si MOF. (f–h) XRD patterns, FT-IR and XPS survey spectra of Ti–Si MOF and MIL-125 (Ti). (i) Crystal structure of $Ti_8O_8(OH)_4$–$(O_2C$–C_6H_4–$CO_2)_6$. (j) DFT calculation simulated crystal structure of $Si_8O_8(OH)_4$–$(O_2C$–C_6H_4–$CO_2)_6$ by replacing Ti in MIL-125 (Ti) with Si. (k) Comparison of crystal structures between $Ti_8O_8(OH)_4$–$(O_2C$–C_6H_4–$CO_2)_6$ and $Si_8O_8(OH)_4$–$(O_2C$–C_6H_4–$CO_2)_6$.

The synthesis procedure of ternary TiO_2/SiO_x@C nanocomposite is schematically illustrated in Fig. 1. First, titanium tetrabutoxide (TBOT), tetraethyl orthosilicate (TEOS) and *p*-phthalic acid (PTA) as the titanium source, silicon source and organic ligand, respectively, were evenly dispersed in a mixed solvent of *N*,*N*-dimethylformamide and methanol in a volume ratio of 4 : 1. After a simple solvothermal process, the Ti–Si MOF was obtained. In this process, TBOT first reacts with PTA to release butanol, which together with methanol react with excess PTA to generate water.[15] Next, the titanium-oxo clusters form and grow *via* the hydrolysis and condensation reaction, and the hydrolysates of TEOS are simultaneously incorporated into titanium-oxo clusters *via* Si–O–Ti bonds.[16] Then, these titanium-oxo clusters further grow to form cyclic octamers that are composed of $Ti(Si)O_5(OH)$ octahedrons by sharing edges and corners.[17] Finally, the cyclic octamers and PTA, are linked through the coordinative bonds to form the precursor of Ti–Si MOF.[18] After the subsequent annealing under nitrogen atmosphere, porous ternary TiO_2/SiO_x@C nanocomposite was synthesized.

To explore the impact of feed ratio of titanium source and silicon source on the formation of Ti–Si MOF, a range of controlled experiments with different feed ratios were designed. A molar feed ratio of titanium source and silicon source at 7 : 3 was selected in order to maximize the silicon content for a higher capacity and also allow a uniform shape (Fig. S1a–f, ESI†). Scanning electron microscopy (SEM) images indicate the formation of Ti–Si MOF with the size ranging from 200 to 500 nm (Fig. 2a). The coexistence of C, O, Ti, and Si in the Ti–Si MOF is verified by the corresponding energy-dispersive X-ray (EDX) mapping images (Fig. 2b–e). X-ray diffraction (XRD) patterns of Ti–Si MOF and MIL-125 (Ti) show no significant difference and their XRD patterns are in accord with the standard data of MIL-125 (Ti), which indicates the identical crystal structure of Ti–Si MOF and MIL-125 (Ti) (Fig. 2f).[18] The Fourier transform infrared (FT-IR) transmittance spectra of Ti–Si MOF and MIL-125 (Ti) show the similar characteristic peaks (Fig. 2g).[19,20] However, an additional peak located at around 950 cm^{-1} belonging to Si–O–Ti bonds appears in the FT-IR spectrum of Ti–Si MOF, which verifies the formation of Ti–Si MOF. Further, the peak intensities around 950 cm^{-1} for the as-synthesized precursors gradually increase with the increasing feeding proportion of silicon source (Fig. S2, ESI†). X-ray photoelectron spectroscopy (XPS) result clearly displays the signal of silicon, which further demonstrates the existence of Si (Fig. 2h). To get further insight of Ti–Si MOF, density functional theory (DFT) simulations were performed to investigate a model coordinative compound (denoted as $Si_8O_8(OH)_4$–$(O_2C$–C_6H_4–$CO_2)_6$) in regard to the connection of silicon-oxo cyclic octamers with PTA. Its crystal structure was illustrated after DFT calculations by using Si to completely replace Ti in MIL-125 (Ti) or $Ti_8O_8(OH)_4$–$(O_2C$–C_6H_4–$CO_2)_6$ (Fig. 2j), and Fig. 2i displays the crystal structure of MIL-125 (Ti). The result shows that the distortion index of the $Si_8O_8(OH)_4$–$(O_2C$–C_6H_4–$CO_2)_6$ (0.04356) is very similar to the distortion index of MIL-125 (Ti) (0.07559) (Fig. 2k), indicating the replacement of Ti with Si leads to negligible structure change and thus favourable formation of Ti–Si MOF.

Thermogravimetric analysis (TGA) reveals that Ti–Si MOF underwent two degradation stages between 20–250 °C and 400–500 °C, which is in accord with the previously reported MIL-125 (Ti) (Fig. S3, ESI†).[20] Besides, N_2 adsorption/desorption isotherms of them show little difference (Fig. S4a, ESI†), and the calculated Brunauer–Emmett–Teller (BET) specific surface area of both are almost the same (1004 $m^2\ g^{-1}$ for MIL-125 (Ti), 1000 $m^2\ g^{-1}$ for Ti–Si MOF). The pore size distribution plots of these MOFs indicate a typical micro-porous material, while partial mesopores with pore diameter of about 6 nm are also present in Ti–Si MOF according to the pore size distribution curve (Fig. S4b, ESI†). These mesopores are suspected to be the defects in the crystal structure due to the partial exchange of Ti and Si.

Further, ternary TiO_2/SiO_x@C nanocomposite was obtained after controlled pyrolysis of Ti–Si MOF precursor, and their morphology and structure were investigated *via* SEM and transmission electron microscopy (TEM). As shown in Fig. 3a–c, the as-synthesized ternary TiO_2/SiO_x@C nanocomposite exhibits as solid spheres and has retained the morphology of the precursor Ti–Si MOF. From Fig. 3d, e and g–l, TiO_2 nanocrystallites with an average size of less than 5 nm and amorphous SiO_x are

 This journal is © The Royal Society of Chemistry 2020

Published on 29 January 2020. Downloaded by WUHAN UNIVERSITY OF TECHNOLOGY on 4/7/2020 9:24:58 AM.

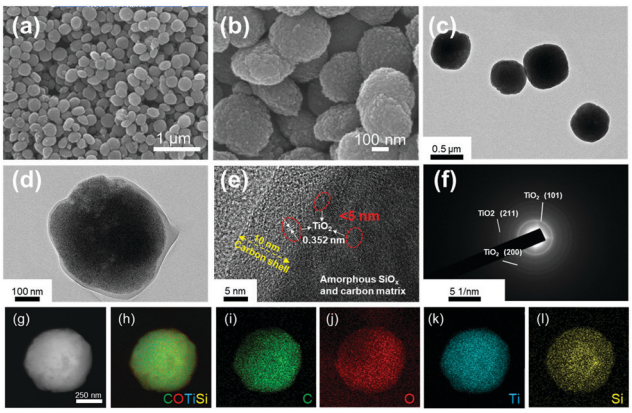

Fig. 3 Characterization of the TiO_2/SiO_x@C nanocomposite. (a and b) SEM images. (c and d) TEM images. (e and f) HRTEM image and SAED pattern. (g) STEM image and corresponding elemental mapping images (h–l) of TiO_2/SiO_x@C.

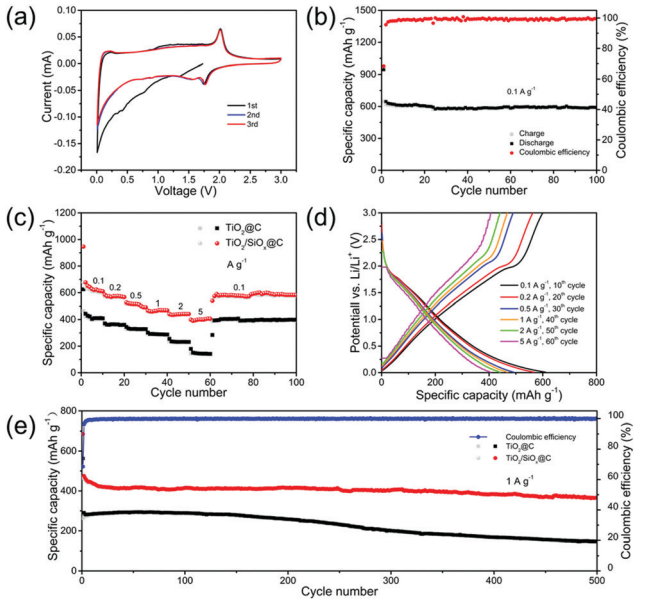

Fig. 4 Lithium storage performances of TiO_2/SiO_x@C and TiO_2@C. (a) The first three CV curves of TiO_2/SiO_x@C at a scan rate of 0.1 mV s^{-1} in 0.01–3.00 V. (b) Cycling performance of TiO_2/SiO_x@C tested at the current density of 0.1 A g^{-1}. (c) Rate performances of TiO_2/SiO_x@C and TiO_2@C. (d) The corresponding charge–discharge curves of TiO_2/SiO_x@C at different current densities. (e) Cycling performance of TiO_2/SiO_x@C and TiO_2@C at a current density of 1 A g^{-1}.

embedded in the carbon matrix to form the inner core, which is encapsulated in a uniform carbon shell with the thickness of about 10 nm. This core–shell structure was formed due to the inconsistent shrinkage rates of different components during the pyrolysis process, which is common in the pyrolysis of MOFs.[21] Excessive aqueous hydrogen fluoride (HF) solution was used to etch TiO_2/SiO_x@C, and above-mentioned conjecture was verified by TEM images of remaining products (Fig. S5a and b, ESI†). The Raman spectrum substantiates the amorphous nature of the carbon component (Fig. S6a, ESI†). The weight fraction of carbon is calculated to be 16.8% through TGA (Fig. S6b, ESI†). As shown in Fig. 3e, the measured fringe spacing of 0.352 nm relates to the (101) plane of anatase TiO_2. Meanwhile, characteristic diffraction rings of anatase TiO_2 are displayed by the selected area electron diffraction patterns (Fig. 3f), which is consistent with the XRD pattern of TiO_2/SiO_x@C in Fig. S7 (ESI†). In contrast, no lattice fringes or diffraction rings related to SiO_x can be observed due to its amorphous feature. In addition, the TiO_2 component in TiO_2/SiO_x@C exhibits purely anatase phase, which is different from that in TiO_2@C which displays both anatase and rutile phases (Fig. S7, ESI†), because SiO_x on the surface of TiO_2 nanocrystallites can improve their thermal stability during the pyrolysis process. The EDX mapping images show that the elements C, O, Ti and Si are evenly distributed (Fig. 3g–l), accounting for 36.89% of C, 38.11% of O, 20.33% of Ti and 4.67% of Si (Table S1, ESI†). Ti 2p spectrum displays two peaks centered at 464.5 and 458.8 eV, which are assigned to Ti^{4+} $2p_{1/2}$ and Ti^{4+} $2p_{3/2}$, respectively (Fig. S8a, ESI†).[22] The Si 2p peak can be simulated to three small peaks located at 103.93, 103.08 and 102.11 eV, which are related to Si^{4+}, Si^{3+} and Si^{2+}.[23] The proportions of different valences of Si are estimated to be 14.7% (Si^{4+}), 63.6% (Si^{3+}) and 21.7% (Si^{2+}) through calculating the respective area of the fitting peaks (Fig. S8b, ESI†). Then, the average valence of Si element in TiO_2/SiO_x@C is inferenced to be +2.93, and the corresponding x value is 1.465. Thus, it can be deduced that TiO_2/SiO_x@C is comprised of 62.4 wt% of TiO_2, 20.8 wt% of $SiO_{1.465}$ and 16.8 wt% of C according to EDX mapping, XPS and TGA results. Besides, Fig. S9a and b (ESI†) show that TiO_2/SiO_x@C has abundant hierarchical pores. The BET surface area is 64.31 m^2 g^{-1} (Fig. S9a, ESI†) and pore sizes are mainly distributed at 0–5 nm, followed by 5–25 nm (Fig. S9b, ESI†).

In order to prove the superiority of the architecture, the as-synthesized TiO_2/SiO_x@C nanocomposite was performed as an anode material for LIBs. From the cyclic voltammetry (CV) curve (Fig. 4a) in the initial discharge process, the cathode peak at 0.75 V relates to the electrolyte deposition and the formation of solid electrolyte interface (SEI) layer.[24] The sloping region below 0.5 V is associated with the formation of Li_2O and Li_4SiO_4.[9,10] The redox pair at 1.75 V and 2.00 V is ascribed to the lithiation/delithiation of anatase TiO_2.[25] The initial discharge/charge specific capacity TiO_2/SiO_x@C are 945/647 mA h g^{-1}, with the corresponding initial coulombic efficiency (ICE) of 68.5% (Fig. S10a, ESI†). Moreover, based on the mass fraction of SiO_x, the reversible capacity contribution of SiO_x in TiO_2/SiO_x@C was calculated to be ~260 mA h g^{-1} (Fig. S10a–c, ESI†). After 100 cycles, TiO_2/SiO_x@C exhibits a reversible capacity of 586 mA h g^{-1} with a high capacity retention of 90.6% (Fig. 4b). From Fig. 4c, TiO_2/SiO_x@C delivers average charge capacities of 615, 567, 507, 465, 439 and 401 mA h g^{-1} at 0.1, 0.2, 0.5, 1, 2 and 5 A g^{-1}, respectively, while TiO_2@C delivers 412, 359, 328, 289, 231 and 144 mA h g^{-1}. Both TiO_2/SiO_x@C and TiO_2@C show good capacity recovery when the current density returns to 0.1 A g^{-1}. The charge–discharge voltage profiles of TiO_2/SiO_x@C at different current densities (Fig. 4d) indicate the characteristics of low polarization and high capacity reversibility. At a current density of 1 A g^{-1}, TiO_2/SiO_x@C displays a high reversible specific capacity of

Published on 29 January 2020. Downloaded by WUHAN UNIVERSITY OF TECHNOLOGY on 4/7/2020 9:24:58 AM.

365 mA h g^{-1} with a 78% capacity retention after 500 cycles, while TiO_2@C retains a low specific capacity of 147 mA h g^{-1} (Fig. 4e). Here, TiO_2@C exhibits degrading long-cycle performance, which could be attributed to the fact that rutile TiO_2 exhibits inferior conductivity than anatase TiO_2 due to less defects and oxygen vacancies and the characteristic that rutile TiO_2 allows only *c*-axis diffusion of Li^+.[26,27] This assumption is also confirmed by electrochemical impedance spectroscopy test (Fig. S11a, ESI†) which shows that TiO_2/SiO_x@C displays better electronic conductivity and faster Li^+ diffusion. The morphology and structure of TiO_2/SiO_x@C were well maintained after 100 cycles at 1 A g^{-1} (Fig. S11b, ESI†). Excellent cycle stability of TiO_2/SiO_x@C was also obtained at 5 A g^{-1} with the reversible capacity retained >300 mA h g^{-1} after 1000 cycles (Fig. S12, ESI†). Moreover, the electrochemical kinetics of TiO_2/SiO_x@C were further characterized and analyzed (Fig. S13a–d, ESI†).

Compared with most TiO_2-based and TiO_2/SiO_x-based anode materials previously reported for LIBs, the MOF-derived TiO_2/SiO_x@C possesses overall excellent electrochemical performances (Table S2, ESI†), which is attributed to the following aspects. First, TiO_2 nanocrystallites and carbon matrix can effectively buffer the volume expansion during lithiation of SiO_x and maintain the stability of ternary nanostructure. Second, SiO_x plays a key role in improving the capacity of whole system due to its high theoretical capacity. Further, the *in situ* generated carbon matrix not only provides effective carbon confinement to TiO_2 and SiO_x to inhibit the aggregation of nanoparticles, but also allow fast electron transport channels. Besides, the derived architecture has hierarchical pores and high specific surface area, which facilitates the rapid transport of Li^+.

In conclusion, a novel Ti–Si MOF precursor was rationally designed and first developed, and the ternary carbon-confined TiO_2/SiO_x@C nanocomposite was obtained after subsequent pyrolysis. When evaluated as an anode material for LIBs, the all-in-one TiO_2/SiO_x@C nanocomposite combines the advantages from synergistic components, and thus delivers a high capacity of 586 mA h g^{-1} at 0.1 A g^{-1} after 100 cycles, a high capacity retention of 78% at 1 A g^{-1} after 500 cycles, and superior rate performance (401 mA h g^{-1} at 5 A g^{-1}). Therefore, the finely-designed TiO_2/SiO_x@C ternary architecture derived from novel titanium–silicon MOF precursor sheds light on the reasonable design of nanocomposites with desired performances for high-efficiency energy storage.

This work was supported by the National Natural Science Foundation of China (21805219, 51521001), the National Key Research and Development Program of China (2016YFA0202603), the Programme of Introducing Talents of Discipline to Universities (B17034), the Yellow Crane Talent (Science & Technology) Program of Wuhan City.

Conflicts of interest

There are no conflicts to declare.

Notes and references

1 X. Tao, J. Wang, Z. Ying, Q. Cai, G. Zheng, Y. Gan, H. Huang, Y. Xia, C. Liang, W. Zhang and Y. Cui, *Nano Lett.*, 2014, **14**, 5288–5294.
2 S. Huang, L. Zhang, X. Lu, L. Liu, L. Liu, X. Sun, Y. Yin, S. Oswald, Z. Zou, F. Ding and O. G. Schmidt, *ACS Nano*, 2017, **11**, 821–830.
3 L. Zeng, C. Zheng, L. Xia, Y. Wang and M. Wei, *J. Mater. Chem. A*, 2013, **1**, 4293–4299.
4 C. Zhang, S. Liu, Y. Qi, F. Cui and X. Yang, *Chem. Eng. J.*, 2018, **351**, 825–831.
5 J. Jiang, S. Liu, Y. Wang, Y. Liu, J. Fan, X. Lou, X. Wang, H. Zhang and L. Yang, *Chem. Eng. J.*, 2019, **359**, 746–754.
6 M. Madian, R. Ummethala, A. O. A. E. Naga, N. Ismail, M. H. Rümmeli, A. Eychmüller and L. Giebeler, *Materials*, 2017, **10**, 678.
7 Y. Chu, J. Feng, Y. Qian and S. Xiong, *RSC Adv.*, 2015, **5**, 40899–40906.
8 X. Li, Y. Chen, H. Yao, X. Zhou, J. Yang, H. Huang, Y.-W. Mai and L. Zhou, *RSC Adv.*, 2014, **4**, 39906–39911.
9 T. Chen, J. Wu, Q. Zhang and X. Su, *J. Power Sources*, 2017, **363**, 126–144.
10 J. Wang, H. Zhao, J. He, C. Wang and J. Wang, *J. Power Sources*, 2011, **196**, 4811–4815.
11 H. Hong, J. Liu, H. Huang, C. Atangana Etogo, X. Yang, B. Guan and L. Zhang, *J. Am. Chem. Soc.*, 2019, **141**, 14764–14771.
12 R. Bi, C. Zeng, H. Huang, X. Wang and L. Zhang, *J. Mater. Chem. A*, 2018, **6**, 14077–14082.
13 S. J. Yang, S. Nam, T. Kim, J. H. Im, H. Jung, J. H. Kang, S. Wi, B. Park and C. R. Park, *J. Am. Chem. Soc.*, 2013, **135**, 7394–7397.
14 W. Sun, S. Chen and Y. Wang, *Dalton Trans.*, 2019, **48**, 2019–2027.
15 L. Rozes, N. Steunou, G. Fornasieri and C. Sanchez, *Monatsh. Chem.*, 2006, **137**, 501–528.
16 C. Gaidau, A. Petica, M. Ignat, L. M. Popescu, R. M. Piticescu, I. A. Tudor and R. R. Piticescu, *Arabian J. Chem.*, 2017, **10**, 985–1000.
17 M. Sabo, W. Böhlmann and S. Kaskel, *J. Mater. Chem.*, 2006, **16**, 2354–2357.
18 Y. Fu, D. Sun, Y. Chen, R. Huang, Z. Ding, X. Fu and Z. Li, *Angew. Chem., Int. Ed.*, 2012, **51**, 3364–3367.
19 P. George, N. R. Dhabarde and P. Chowdhury, *Mater. Lett.*, 2017, **186**, 151–154.
20 Y. An, H. Fei, Z. Zhang, L. Ci, S. Xiong and J. Feng, *Chem. Commun.*, 2017, **53**, 8360–8363.
21 J. Meng, Q. He, L. Xu, X. Zhang, F. Liu, X. Wang, Q. Li, X. Xu, G. Zhang, C. Niu, Z. Xiao, Z. Liu, Z. Zhu, Y. Zhao and L. Mai, *Adv. Energy Mater.*, 2019, **9**, 1802695.
22 H. He, Q. Zhang, H. Wang, H. Zhang, J. Li, Z. Peng, Y. Tang and M. Shao, *J. Power Sources*, 2017, **354**, 179–188.
23 Z. Li, H. Zhao, P. Lv, Z. Zhang, Y. Zhang, Z. Du, Y. Teng, L. Zhao and Z. Zhu, *Adv. Funct. Mater.*, 2018, **28**, 1605711.
24 P. Verma, P. Maire and P. Novák, *Electrochim. Acta*, 2010, **55**, 6332–6341.
25 Z. Wang, X. Li, H. Xu, Y. Yang, Y. Cui, H. Pan, Z. Wang, B. Chen and G. Qian, *J. Mater. Chem. A*, 2014, **2**, 12571–12575.
26 D. Deng, M. G. Kim, J. Y. Lee and J. Cho, *Energy Environ. Sci.*, 2009, **2**, 818.
27 T. Sarkar, K. Gopinadhan, J. Zhou, S. Saha, J. Coey, Y. P. Feng and T. Venkatesan, *ACS Appl. Mater. Interfaces*, 2015, **7**, 24616–24621.

 This journal is © The Royal Society of Chemistry 2020